International Journal of Machine Tools & Manufacture 109 (2016) 126–136

Contents lists available at ScienceDirect

International Journal of Machine Tools & Manufacture

journal homepage: www.elsevier.com/locate/ijmactool

Crack-free ductile mode grinding of fused silica under controllable dry grinding conditions

Wei Wang [a,b], Peng Yao [a,b,*], Jun Wang [c,*], Chuanzhen Huang [a,b], Hongtao Zhu [a,b], Bin Zou [a,b], Hanlian Liu [a,b], Jiwang Yan [d]

[a] Center for Advanced Jet Engineering Technologies (CaJET), School of Mechanical Engineering, Shandong University, Jinan, Shandong 250061, China
[b] Key Laboratory of High Efficiency and Clean Mechanical Manufacture, Ministry of Education, PR China, Jinan, Shandong 250061, China
[c] School of Mechanical and Manufacturing Engineering, University of New South Wales, Sydney, New South Wales 2052, Australia
[d] Department of Mechanical Engineering, Keio University, Yokohama 223-8522, Japan

ARTICLE INFO

Article history:
Received 16 May 2016
Received in revised form
14 July 2016
Accepted 19 July 2016
Available online 21 July 2016

Keywords:
Fused silica
Ductile mode grinding
High temperature nanoindentation
Material densification
Grinding temperature
Infrared radiation

ABSTRACT

A crack-free ductile mode grinding of fused silica was realized by a controllable dry grinding process in this research, which is attributed to the improvement of fused silica's ductile machinability induced by the high grinding temperature. The plastic deformation of fused silica consists of shear flow and densification. Plastic deformation mechanisms and cracking behaviors related to densification were investigated firstly by high temperature nanoindentation experiments to reveal the ductile–brittle transition mechanisms. Fused silica exhibits less densification and more shear flow at high temperature than room temperature. The critical ductile–brittle transition load of fused silica is higher at high temperature than room temperature. These results may lead to the improvement of the fused silica's ductile machinability at high temperature. Dry grinding experiments were conducted to investigate the effect of grinding depth. A mathematical model is established to predict the maximum temperature in workpiece. A novel infrared radiation (IR) transmission on-line measurement method was presented to acquire the workpiece temperature in the contact zone directly. The predicted results coincide well with the experiment results. Contrary to the conventional experience, a large grinding depth is beneficial for the surface quality and integrity in the dry grinding of fused silica due to the increased grinding temperature; however, the excessive grinding depth results in grinding wheel burn. The ductile grinding depth of the fused silica increases from sub-micrometers to 5 μm by dry grinding which makes the grinding process more controllable and effective.

© 2016 Elsevier Ltd. All rights reserved.

1. Introduction

Amorphous silicon dioxide, i.e., fused silica, is an excellent lens and window material for ultraviolet laser transmission in photolithographic applications, high-peak-power laser fusion facilities and space telescopes for its high ultraviolet transmission, low expansion coefficient and high laser damage threshold [1]. Currently, fused silica lenses are finished by grinding, lapping and polishing. The polishing process costs over 60% of the entire production cycle [2]; thus, it is important to produce higher surface integrity in the grinding process to reduce the polishing time and the cost of production.

Ductile mode grinding of hard and brittle materials is an attractive method for efficiently generating a surface with nanometer or sub-nanometer level surface roughness. It is widely recognized hard and brittle materials could be machined in ductile mode if the undeformed chip thickness were controlled to be small enough [3].

Single-crystal silica, ceramics and most optical glass are reported to be grindable in ductile mode with a grinding depth of several micrometers using precision machine tools [4–6]. However, it is extremely difficult to grind fused silica in ductile mode without causing any cracks. Taper grinding experiments on fused silica surfaces without damage demonstrated that critical grinding depth of the ductile–brittle transition was 0.2 μm [7]. The extremely narrow range of critical depth makes the crack-free ductile mode grinding of fused silica uncontrollable and inefficient. Many efforts for ductile grinding of fused silica, including electrolytic in-process dressing(ELID) [8], using ultra-fine grits wheels [9] or truncation coarse grain wheels [10], succeed to reduce the roughness and sub-surface damage (SSD) depth of fused silica, while failed to produce an ultra-smooth fused silica surface

* Corresponding authors at: Center for Advanced Jet Engineering Technologies (CaJET), School of Mechanical Engineering, Shandong University, Jinan, Shandong 250061, China.
E-mail addresses: yaopeng@sdu.edu.cn (P. Yao), jun.wang@unsw.edu.au (J. Wang).

http://dx.doi.org/10.1016/j.ijmachtools.2016.07.007
0890-6955/© 2016 Elsevier Ltd. All rights reserved.

Downloaded from Yan Laboratory, Keio University at http://www.yan.mech.keio.ac.jp. Redistribution is subject to copyright licence from the journal publisher.

Nomenclature

d_c	critical chip thickness
E	Young's modulus
H	hardness
K_c	fracture toughness
v_s	wheel speed
v_w	workpiece feed rate
Δ	grinding depth
g_m	undeformed chip thickness
R_D	section area ratio of sink-in to indenter
S_a	actual section area of indentation
S_i	the calculated section area of the indenter
$\bar{q}$	average heat power density
b	width of the grinding wheel
c	specific heat
D	diameter of grinding wheel
θ	temperature rise
l	geometrical wheel workpiece contact length
ε	ratio of heat power into the workpiece
λ	thermal conductivity
ρ	density
F_0	tangential grinding force per unit equivalent grinding thickness
a_{ep}	equivalent grinding thickness

without any surface and sub-surface cracks in controllable conditions.

Brittle–ductile transition in machining of hard brittle materials is a complex interaction of tool (grain) geometry, processing parameters, environmental conditions (temperature and humidity), material properties, et al. [11]. The factors affecting the transition are generally divided into two types: external factors, such as stress condition and strain rate et al., and internal factors, such as material properties. Actually tool (grain) geometry, processing parameters et al. affect the brittle–ductile transition through the variation of stress condition and strain rate while the environmental conditions affect through changing the intrinsic material properties.

Without considering the external factors, Bifano presented a model indicating the relationship between the critical ductile–brittle transition chip thickness d_c and intrinsic material properties Young's modulus E, hardness H and the fracture toughness K_c [9]:

$$d_c \propto \left(\frac{E}{H}\right)\left(\frac{K_c}{H}\right)^2 \tag{1}$$

The E, H and K_c of fused silica are 72 GPa, 7.3 GPa, 1.3 MPa m$^{1/2}$, respectively [12]. For comparation, the E, H and K_c of soda-lime-silica glass are 70 GPa, 5.7 GPa, 0.6 MPa m$^{1/2}$, respectively [13]. According to Eq. (1) the calculated d_c of fused silica is much larger than that of soda-lime-silica glass. Nevertheless, the ductile machining of fused silica is actually much more difficult than soda-lime-silica.

Hardness is the plastic deformation resistance of material. However, it does not shed light on the mechanism of permanent deformation of glass under stress, which can be primarily divided into two modes: volume-conservative plastic (or shear) flow and volume contraction densification [14]. Fused silica is called anomalous glass [15] due to its predominant densification under stress. In ductile mode grinding, the material is removed by shear flow while densification has no contribution to chip removal. Thus hardness in Eq. (1) cannot characterize the glasses' ductile machinability.

The fracture toughness, which is also called fracture resistance is calculated by the following equation:

$$K_C = \left(\frac{E}{H}\right)^{0.5}\left(\frac{P}{c}\right)^{1.5} \tag{2}$$

where c is the lengths of radial cracks in indentation.

Densification causes fused silica to act differently in cracking behaviors compared to normal glass [16]. It tends to initiate cone cracks around the impression while the normal glass trend to initiate radial cracks. The radial cracks' lengths of fused silica are always shorter than that of a normal glass [17]. Nevertheless, it is more difficult to grind fused silica in ductile mode on contrary. Thus toughness in Eq. (1) cannot characterize the glasses' fracture resistance. It has been concluded that the plastic deformation and cracking behaviors of glass have a strong relationship with densification [18–20].

Michel et al. [12] experimentally investigated the effects of temperature on hardness and crack nucleation of fused silica during Vickers indentation under the loads of 5 N and 40 N. Comparing with room temperature, the radial crack length and the threshold for the cone cracks of fused silica increase at high temperature. Shear flow is responsible for the residual stress due to the elastic/plastic mismatch [21] whereas densification is not. The radial cracks propagate during the unloading process due to the residual stress induced by shear flow. We can infer that high temperature may improve the ductile machinability of fused silica for its more shear flow based on Michel's study. However, deformation mechanisms and cracking behaviors under nanoindentation below 500 mN which more closely approximates to the load on a single grain in the actual grinding process need further investigation.

This paper presents a dry grinding process using a vitrified bond CBN grinding wheel with high temperature resistance to achieve crack-free ductile mode grinding of fused silica. The high temperature induced by grinding heat improves the ductile machinability of fused silica. Instead of an extremely narrow chip thickness for ductile grinding with coolant, a large grinding depth makes the proposed process more controllable and effective. The physical and chemical properties of fused silica are stable at high temperatures. The annealing point of it is 1200 °C while the softening point is 1600 °C. It cannot be oxidized at high temperatures; thus, the grinding burn of fused silica will not occur at extremely high grinding temperatures during dry grinding. Plastic deformation mechanisms and cracking behaviors related to the densification are investigated firstly by high temperature nanoindentation experiments below 500 mN to reveal the ductile–brittle transition mechanisms. Dry grinding experiments are conducted to investigate the effect of grinding depth for its significance of processing efficiency. A mathematical model is established to predict the maximum temperature at grinding zone. A novel infrared radiation (IR) transmission on-line measurement method was presented to acquire the workpiece temperature in the contact zone directly during surface grinding process.

2. Experiments

The specimens are high purity synthetic fused silica with a transmission wavelength of 0.175–2.5 μm. This type of fused silica is particularly developed for ultraviolet laser transmission. The size of the specimens is ϕ20 mm × 1.5 mm.

Table 1
High temperature indentation parameters.

Species	Temperature (°C)	Load (mN)	Loading/unloading time (s)	Dwell time (s)
Fused silica	20, 150, 300, 450	10, 50, 100, 500	10	15
Soda-lime-silica	20	10, 50, 100, 500	10	15

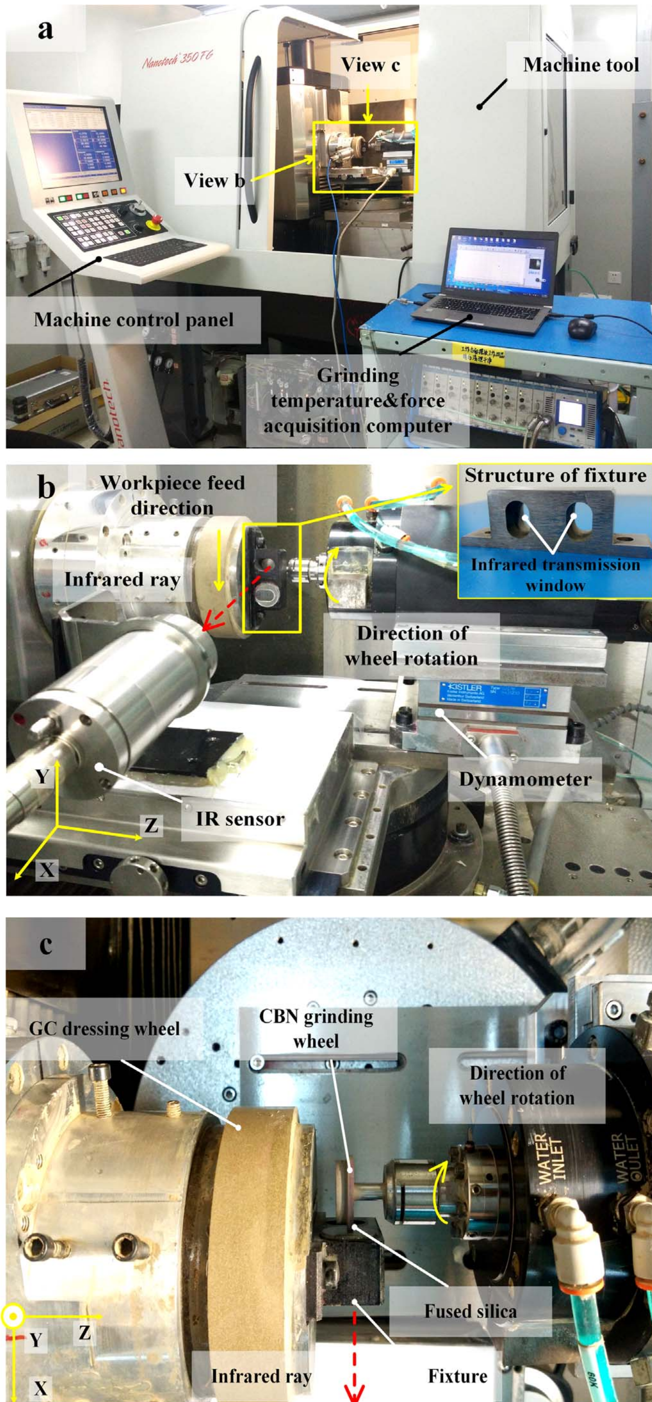

Fig. 1. Set-up for grinding experiments. (a) Global structure. (b) Partial structure from view b. (c) Partial structure from view c.

Table 2
Dry grinding experimental parameters.

No.	Grinding depth Δ (μm)	Wheel speed v_s (m/s)	Workpiece feed rate v_w (mm/min)	Undeformed chip thickness[a] g_m (nm)
1	1	26	200	22
2	3	26	200	39
3	5	26	200	50
4	7	26	200	59

[a] Undeformed chip thickness $g_m = 2a\left(v_w/v_s\right)\sqrt{\Delta/D}$ [22].

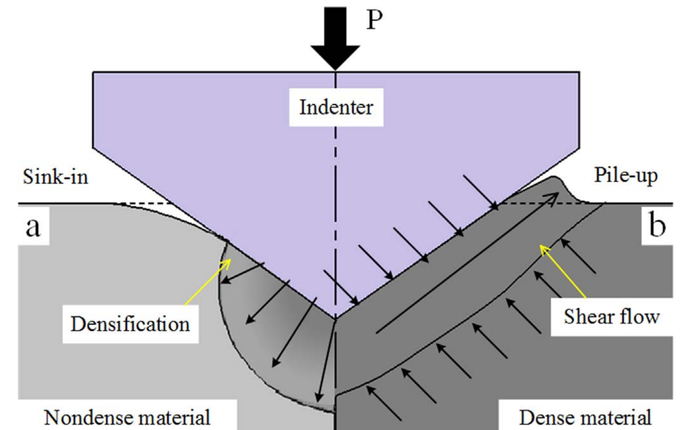

Fig. 2. Schematic of densification and shear flow generation. (a) Situation of sink-in with nondense material. (b) Situation of pile-up with dense material.

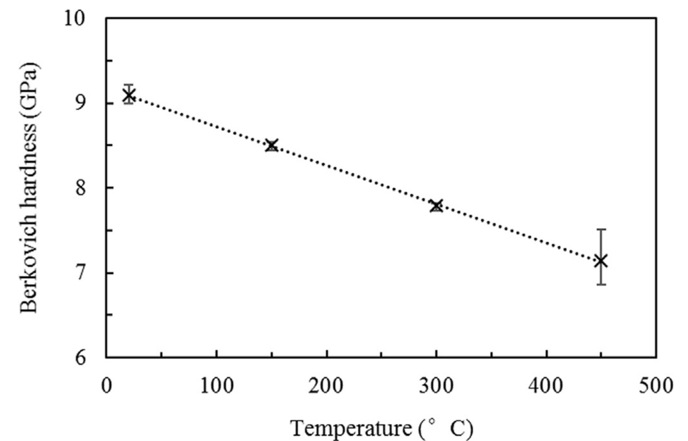

Fig. 3. Variation of Berkovich hardness with temperature for fused silica.

High temperature nanoindentations were performed with a diamond Berkovich indenter by the Micro Materials NanoTest system using a high temperature stage. Both the sample stage and the indenter were separately heated to ensure no heat flow occurs during indentation at a high temperature (isothermal contact). Soda-lime-silica glass, a kind of normal glass, was chosen to comparing with fused silica at room temperature in this experiment. Before the experiments, the specimens were polished to entirely remove the surface and the subsurface damage. The roughness Ra of the specimens was controlled to within 1 nm. The experimental parameters are listed in Table 1. Five indentations were performed under each parameter. The indentations were observed by an atomic force microscopy (AFM) and scanning electron microscope (SEM).

The grinding experiments were performed on an ultra-precision machining system Moore Nanotech 350. The grinding experiment set-up is illustrated in Fig. 1. A GC dressing wheel was

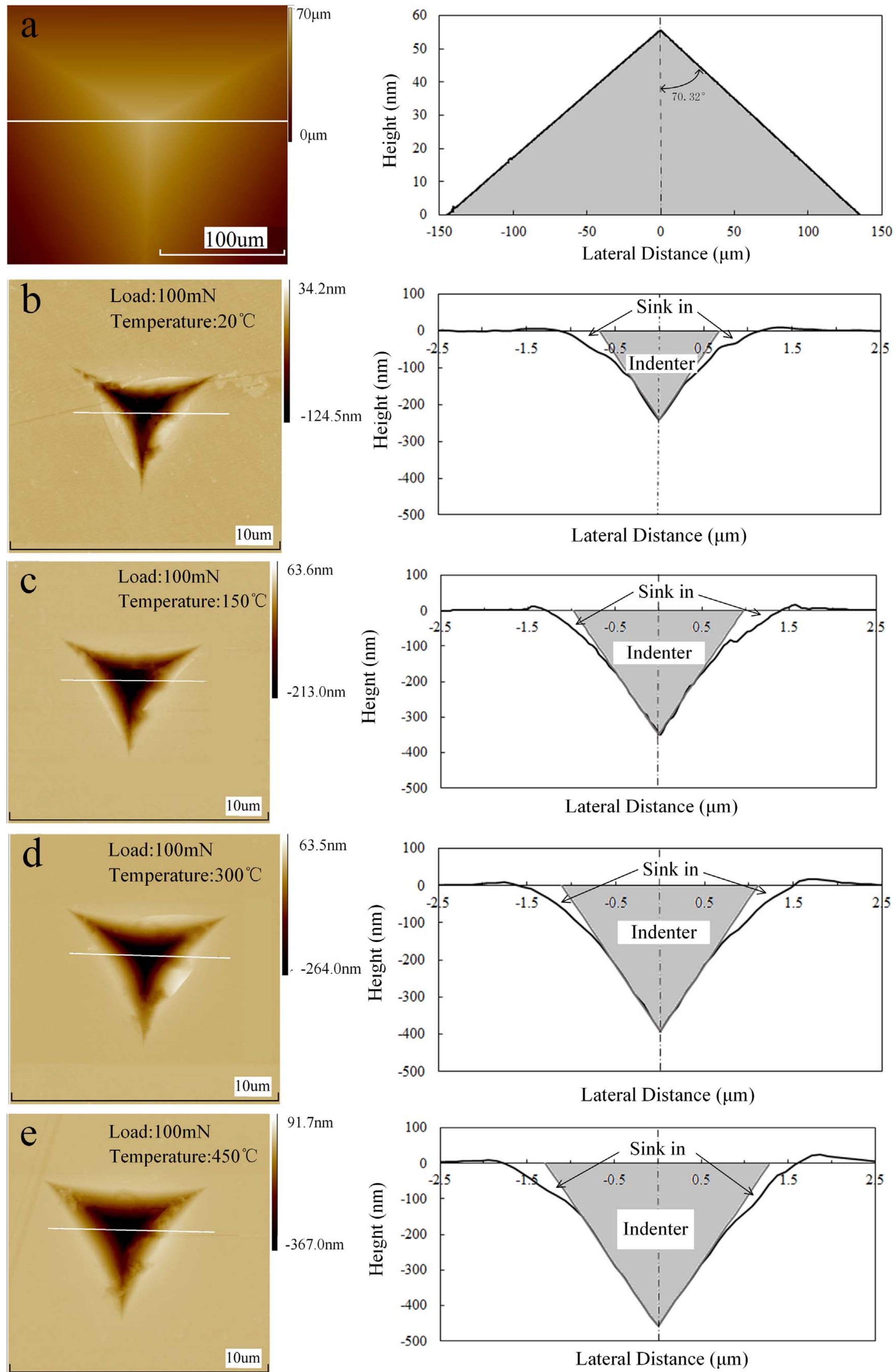

Fig. 4. Comparation of the cross-sectional curves of indenter tip and resulting indenting under 100 mN. (a) Berkovich indenter, and indents obtained at (b) room temperature, (c) 150 °C, (d) 300 °C, (e) 450 °C.

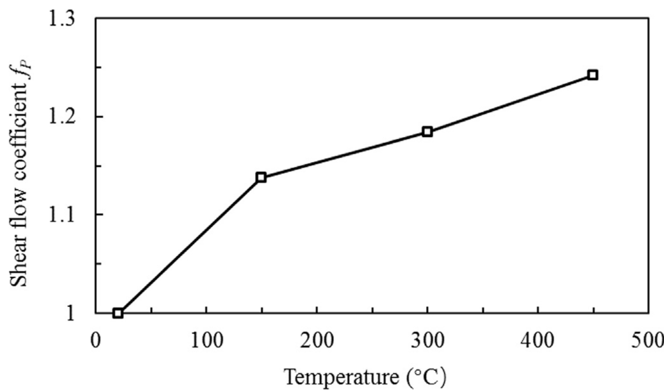

Fig. 5. Variation of the shear flow coefficient f_P with temperature.

fixed on the spindle to make the on-machine dressing of grinding wheel. The spindle would rotate during the dressing process while be locked during the grinding process. A fixture with a hole as IR transmission window was fasten on the end face of the dressing wheel. The fused silica was bonded on the hole and an IR sensor with laser aiming was fixed behind the window to acquire the IR signal during the grinding process. The response wavelength of the IR sensor is 2.3 μm. Fused silica is an excellent material for IR window and its transmissivity at the wavelength of 2.3 μm is 0.95. The fused silica surface measured in grinding experiments was nontransparent because of the micro cracks on the rough ground surface, the other side was well polished and transparent. Hence, the infrared ray emitted from the wheel–workpiece interface could transmit through the internal part and the polished surface of fused silica, and be acquired by the IR sensor. The temperature of workpiece in the contact zone could be measured directly by the IR sensor in consequence. A dynamometer Kistler 9257B was fasten under the air bearing spindle to measure the grinding forces.

A vitrified bond CBN grinding wheel with high temperature resistance was used in the experiments. The average grain size of the wheel was 5 μm. The wheel's diameter and width were 25 mm and 3 mm, respectively. The grinding wheel was well dressed to a radial runout error below 1 μm. After the dressing a dynamic balance was adjusted to retain a wheel vibration under 2 nm during grinding. The dry grinding experiments were conduct on a rough ground surface in brittle mode (Ra=0.17 μm, Rz=1.11 μm, SSD depth=3.56 μm). The grinding parameters are listed in Table 2 .The grinding process was up cut, i.e., the speed directions of the wheel and workpiece were opposite.

After the grinding experiments, a 3D laser confocal microscope Keyence VK-X200K was used to measure the surface morphologies and the roughness of the ground surface. The roughness was randomly measured three times, and the average values were calculated. Elastic Emission Machining was conducted to polish the ground surface for measuring the subsurface damage (SSD) depth [7]. The SSD depth was measured 3 times, and the maximum values were selected.

3. Results and discussion

3.1. The ductile machinability at room temperature and high temperature

3.1.1. Analysis of deformation mechanisms

The Berkovich hardness of fused silica with an increasing temperature measured by the Oliver–Pharr method under the load of 500 mN is indicated in Fig. 3. The hardness of fused silica at room temperature was 9.09 GPa and decreased to 7.14 GPa at 450 °C. As illustrated in the Introduction, the hardness is the plastic deformation resistance of material. Thus the decrease of hardness indicates that the plastic deformation is easier for fused silica at high temperature.

However, the permanent deformation of glass under stress can be divided primarily into shear flow and densification. At the molecular scale, the opened structure of the glass network and more atomic cavities make the fused silica not densified. Thus it always exhibits more densification behaviors under the hydrostatic compression. The densification volume ratio for fused silica is up to 92% in Vickers indentation under the load of 100 mN [21]. In ductile mode grinding, the material is removed by shear flow while densification has no contribution. Hence the decrease of hardness does not equal to the shear flow is easier for fused silica at high temperature.

It is reported the fused silica exhibits an anomalous volume-temperature behavior. The volume reduces while the density increases with the increasing temperature until 1550 °C [23]. It suggests the fused silica become denser at high temperature than room temperature. Hence it can be concluded the fused silica would exhibit less densification at high temperature. Combined with the decrease of hardness, it can be inferred shear flow is easier for fused silica at high temperature which would contribute to material removal in ductile mode. This inference is investigated by the high temperature nanoindentation.

In the nanoindentation experiments, permanent microscopic deformation events aiming at efficiently relaxing the contact stress by increasing the contact surface area will initiate in a process zone near the indenter tip as indicated in Fig. 2 [21]. If the material is dense, the material under the indenter is resistance to the flow material motion, so the material moves to the surface causing pile-up. However, for the fused silica, densification occurs in the hydrostatic compression field out of the indenter-material contact regime. The material moves downwards into the material and sink-in is observed [24,25]. The extent of sink-in will thus depend on the densification for fused silica.

In order to compare the deformation mechanism of fused silica at room temperature and high temperature, the indentations under the load of 100 mN were scanned by AFM. The indentation section curve across of the indentation tip and parallel to the borderline is compared with the cross section curve of indenter as indicated in Fig. 4. Fig. 4(a) indicates the Berkovich indenter cross section curve. The equivalent half cone angle of Berkovich indenter is 70.32°. Fig. 4(b)–(e) compare the cross-section curves of actual indentations with the calculated indenter from room temperature to 450 °C. The penetration depths increase with the temperature which indicates more plastic deformation.

In this study, we define R_D as the area ratio of sink-in to indenter, R_D is calculated by the following equation:

$$R_D = \frac{S_a - S_i}{S_i} \tag{3}$$

where S_a is the actual cross-section area of the indentation; S_i is the calculated cross-section area of the indenter at the same contact depth. Actually R_D is not only determined by the densification but also by the plastic deformation. Since the plastic deformation consisted of densification and shear flow, the extent of densification R_P should be calculated by the following equation:

$$R_P = 1 - R_D = 1 - \frac{S_a - S_i}{S_i} \tag{4}$$

Nevertheless, the value of R_D and R_P have no absolute significance of evaluating the extent of densification and plastic. It is clear that the larger R_D is related to more densification while the

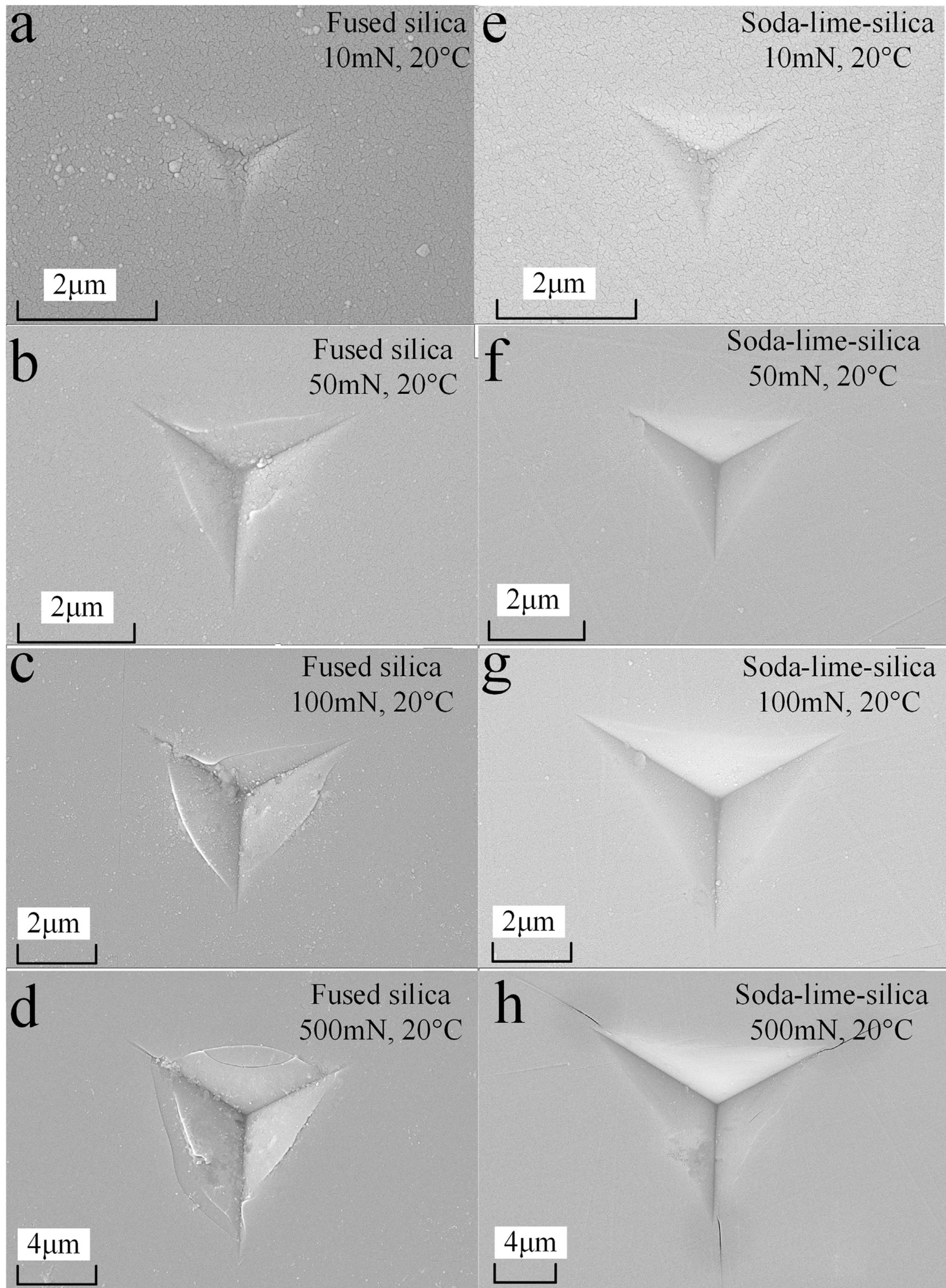

Fig. 6. SEM photographs of nanoindentations under load from 10 mN to 500 mN at room temperature of fused silica and soda-lime-silica. (a) 10 mN of fused silica. (b) 50 mN of fused silica. (c) 100 mN of fused silica. (d) 500 mN of fused silica. (e) 10 mN of soda-lime-silica. (f) 50 mN of soda-lime-silica. (g) 100 mN of soda-lime-silica. (h) 500 mN of soda-lime-silica.

larger R_P is related to more shear flow. Therefore, they should be compared relatively with each other at different temperatures. The shear flow coefficient f_P which is used to investigate the relative variation of shear flow with the increasing temperature is calculated as following:

$$f_P = \frac{R_P}{R_{Pr}} \tag{5}$$

where the R_{Pr} is the R_P at room temperature, i.e., 20 °C. The Eq. (5) has significance only if $S_a > S_i$, i.e., the sink-in exists. The variation

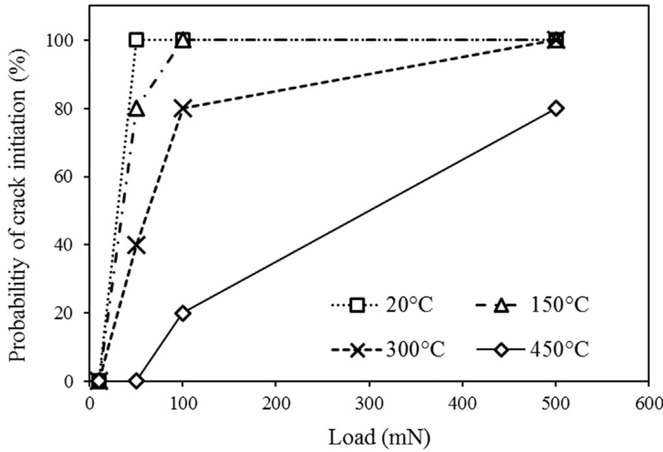

Fig. 7. Probability of crack initiation under different loads.

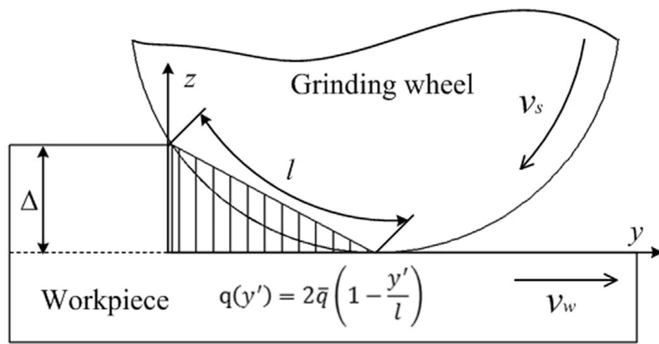

Fig. 8. Schematic diagram of triangular heat source [26].

Table 3
Thermal properties of fused silica and CBN.

Property	Unit	Value	
		Fused silica	CBN
Density (ρ)	kg/m^3	2201	3490
Thermal conductivity (λ)	W/m °C	1.4	20
Specific heat (c)	J/kg °C	800	793

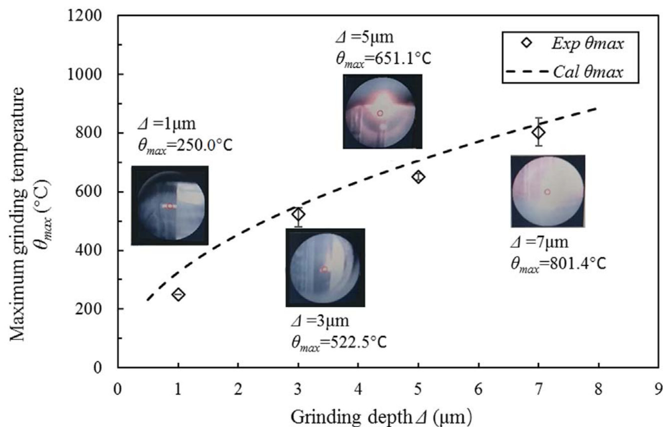

Fig. 9. Comparison of the experimental and predicted maximum temperature in workpiece.

of f_P with temperature is indicated in Fig. 5. f_P is 1 at room temperature defined as the comparative standard, while it increases to 1.24 at 450 °C. It indicates that high temperature improves the shear flow of fused silica.

3.1.2. Analysis on cracking behaviors

The microfracture behaviors of fused silica were compared firstly with soda-lime-silica glass by nanoindentation experiments below 500 mN at room temperature in this research. As indicated in Fig. 6 , no crack is observed on the surface of fused silica under the load of 10 mN. Borderline cracks along the impression initiate when the load is 50 mN. For the soda-lime-silica glass, no crack is observed on the surface until 100 mN. Radial cracks initiate under the load of 500 mN in one indentation. There is still no crack on the surface of the rest 4 indentations. It can be concluded the critical ductile–brittle transition load for fused silica is much lower than soda-lime-silica glass. Actually, the atomic cavities in fused silica are flaws of the material at the molecular scale. The cracks will nucleate from the cavities easily during loading process.

Different with Michel's study under high load, the microfracture behaviors of fused silica at high temperature were investigate by nanoindentation under the load below 500 mN. The probability of crack initiation with increasing loads at different temperatures are compared in Fig. 7. There is always no crack under the load of 10 mN at any temperature. At room temperature, 100% indentations initiate cracks on the surface when the load is more than 50 mN. The probability of crack initiation decrease with the increasing temperature. The probability is only 80% at the temperature of 450 °C. The probability of crack initiation at high temperature are almost lower than that at room temperature. High temperature improves the critical ductile–brittle transition load of fused silica for the less atom cavities induced by more densified molecular structure.

Based on the results and discussion in Sections 3.1.1 and 3.1.2, it can be concluded high temperature may lead to improvement of the fused silica's ductile machinability.

3.2. The maximum workpiece temperature at contact zone

The temperature field at the grinding zone can be calculated by considering the wheel–workpiece interface as a band moving heat source. The power density of the heat source follows a triangular distribution, as indicated in Fig. 8 [26].

The average heat power density is $\bar{q}$. The heat source length is the contact length of the geometrical wheel workpiece l. The heat source moves along the y-axis at the workpiece feed rate v_w. The heat power of a point y' at the grinding zone can be calculated as follows:

$$q(y')=2\bar{q}\left(1-\frac{y'}{l}\right) \tag{6}$$

The workpiece temperature $\theta_{(y,z)}$ at a point (y, z) is:

$$\theta_{(y,z)} = \frac{\bar{q}\sqrt{y}}{\sqrt{k_w(c\rho)_w}\sqrt{\pi}\sqrt{v_w}}\cdot\left[4-\frac{8}{3}\frac{y}{l}-\frac{2}{3}\frac{v_w z^2}{k_w l}\right]e^{-\frac{z^2 v_w}{4k_w y}} + \frac{\bar{q}z}{k_w(c\rho)_w}\left[\frac{v_w z^2}{3k_w l}-2\left(1-\frac{y}{l}\right)\right]erfc\left(\frac{z\sqrt{v_w}}{\sqrt{4k_w y}}\right) \tag{7}$$

where c is specific heat; ρ is density; $k=\frac{\lambda}{c\rho}$; λ is thermal conductivity. The subscript w is workpiece, fused silica. $erfc(s)$ is error compensation function.

The maximum temperature θ_{max} can be obtained at the median point of the surface at the wheel–workpiece interface $\left(z = 0,\ y=\frac{l}{2}\right)$ as follows:

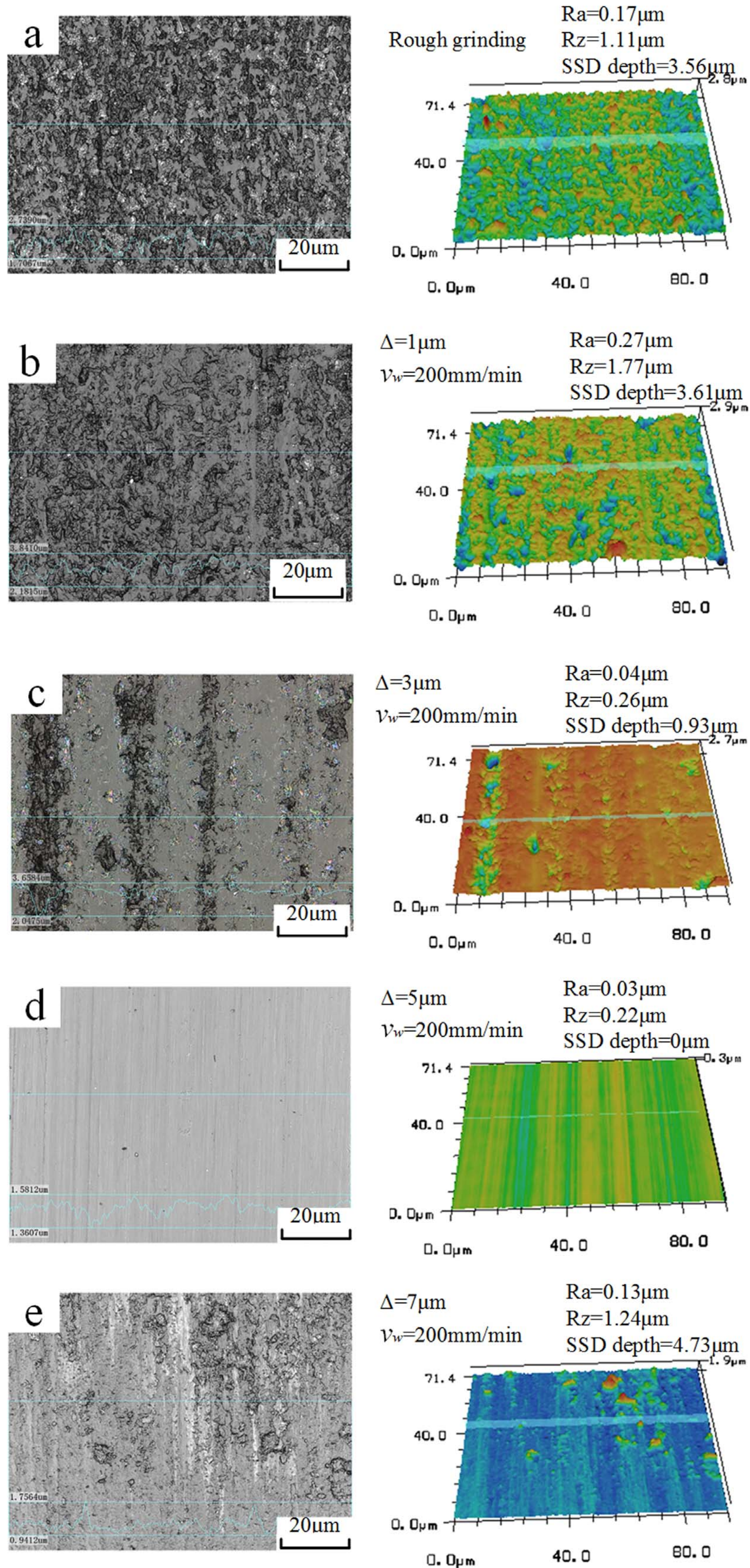

Fig. 10. 2D and 3D Morphologies of the fused silica surface in different grinding conditions. (a) Rough grinding. (b) $\Delta = 1$ μm. (c) $\Delta = 3$ μm. (d) $\Delta = 5$ μm. (e) $\Delta = 7$ μm.

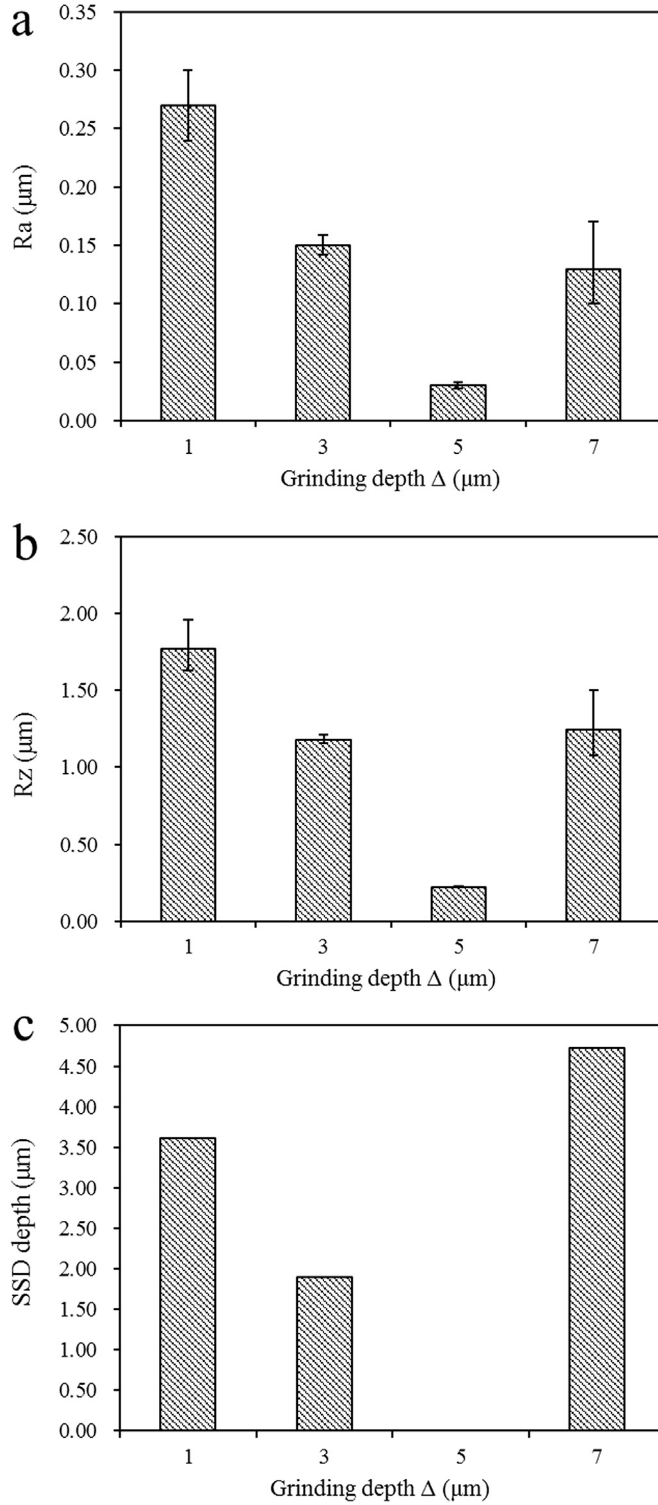

Fig. 11. Surface roughness and SSD depth of the fused silica at different grinding depth. (a) Ra. (b) Rz and, (c) SSD depth.

$$\theta_{max} = \frac{4\sqrt{2}\bar{q}}{3\left(\sqrt{k}c\rho\right)_w \sqrt{\pi}}\sqrt{\frac{l}{v_w}} \tag{8}$$

The geometrical wheel workpiece contact length l can be given as follows:

$$l = \sqrt{\Delta \cdot D} \tag{9}$$

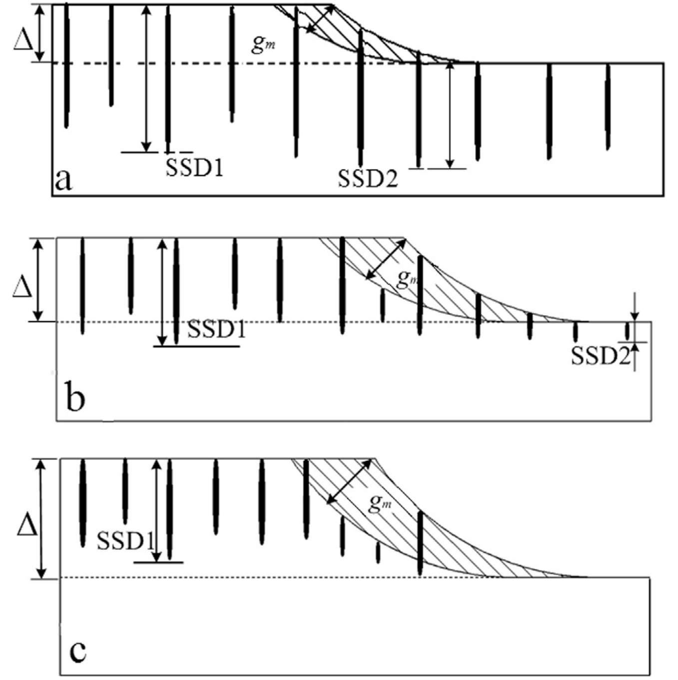

Fig. 12. Illustration of grinding process at different grinding conditions. (a) Brittle grinding $\Delta < \text{SSD1}$. (b) Semi-ductile grinding $\Delta < \text{SSD1}$. (c) Ductile grinding $\Delta > \text{SSD1}$.

where Δ is the grinding depth; and D is the diameter of the grinding wheel. By substituting Eq. (9) into Eq. (8), we can obtain

$$\theta_{max} = 1.06\frac{\bar{q}\Delta^{1/4}D^{1/4}}{\left(k^{1/2}c\rho\right)_w v_w^{1/2}} \tag{10}$$

The total heat power density q_t at grinding zone is calculate as [27]:

$$q_t = \frac{F_t v_s}{bl} \tag{11}$$

where b is the grinding wheel width; F_t is the tangential grinding force. Bus presented that F_t has the flowing relationship with the equivalent grinding thickness $a_{ep}\left(a_{ep} = \frac{v_w}{v_s}\Delta\right)$[28]:

$$F_t = F_0 a_{ep}^f \tag{12}$$

where F_0 is a constant that the tangential grinding force in per unit equivalent grinding thickness. f is an index between 0.4 and 0.9.

In the dry grinding process, the ratio of the heat power into the workpiece ε can be calculated using Ramanath's model [29] as follows:

$$\varepsilon = \left(1 + \frac{(k\rho c)_s}{(k\rho c)_w}\right)^{-1} \tag{13}$$

Thus, the average heat power density $\bar{q}$ can be given as follows:

$$\bar{q} = \varepsilon q_t = F_0\left(1 + \frac{(k\rho c)_s}{(k\rho c)_w}\right)^{-1} \cdot \frac{v_w^f v_s^{(1-f)}\Delta^{(f-1/2)}}{bD^{1/2}} \tag{14}$$

By substituting Eq. (14) into Eq. (10), the relationship between the maximum temperature in workpiece and the grinding parameters can be given as follows:

$$\theta_{max}=1.06F_0\left(1+\frac{(k\rho c)_s}{(k\rho c)_w}\right)^{-1}\cdot\frac{v_w^{(f-1/2)}v_s^{(1-f)}\Delta^{(f-1/4)}}{\left(k^{1/2}c\rho\right)_w bD^{1/4}} \tag{15}$$

By measuring the grinding force, F_0 and f in this study can be calculated: $f=0.73$; $F_0=1.013\times10^7$ N/m$^{0.73}$. Other parameters needed for calculating the grinding temperature are listed in Table 3. Fig. 9 compares the measured and predicted the maximum temperature at the dry grinding zone with different grinding depth. The grinding temperatures were measured 3 times with each grinding depth and the average values were calculated.

The results demonstrated that the predicted grinding temperature shows good agreement with the measured values both in magnitude and variation trend. The relative errors between the experimental and calculated temperature were less than 10%. This has proved the validity of the proposed grinding temperature model.

3.3. Effect of grinding depth in dry grinding experiments

3.3.1. Surface morphologies and integrity

The ground surface morphologies observed by a 3D laser confocal telescope are illustrated in Fig. 10. The roughness and SSD depth are indicated in Fig. 11. Fig. 10(a) indicates the morphologies of rough grinding surface. Fig. 10(b)–(e) indicates the morphologies of surfaces with different grinding depth.

As indicated in Fig. 10(b), the surface was ground with a 1 μm grinding depth. The morphologies appear to be similar to the surface after rough grinding as shown in Fig. 10(a). A multitude of micro cracks are distributed uniformly on the surface. No streaks induced by the grits can be found. The roughness of the surface (Ra=0.27 μm, Rz=1.77 μm) appears even worse than that of the surface after rough grinding. The SSD depth measured using the polishing method is 3.61 μm, which is nearly equal to that after rough grinding. The material is clearly removed in entire brittle mode.

The surface ground with a grinding depth of 3 μm is illustrated in Fig. 10(c). Grinding streaks can be observed. The surface roughness (Ra=0.04 μm, Rz=0.26 μm) is improved compared to that after rough grinding. The SSD depth is 1.90 μm, which is considerably reduced. Both the number and the depth of the micro cracks decrease when compared to rough grinding. Hence, it is considered to be a semi-ductile mode grinding.

The surface ground with a grinding depth of 5 μm is shown in Fig. 10(d). A series of grinding streaks are clearly observed on the surface. A superior surface quality (Ra=0.03 μm, Rz=0.22 μm) without any cracks is observed. No subsurface micro cracks were exposed after polishing. The material is removed in the ductile mode without a crack.

The surface ground with a grinding depth of 7 μm is shown in Fig. 10(e). The grinding temperature was excessively high (801.4 °C) and burned the wheel. The friction between the binder and the workpiece surface results in a poor quality and integrity (Ra=0.13 μm, Rz=1.24 μm and SSD depth=4.73 μm).

3.3.2. Surface generation mechanisms

Fig. 12 illustrates the surface generation mechanisms in different grinding parameters. The grinding depth of 1 μm is much smaller than the subsurface damage depth induced by rough ground in fused silica (SSD1). Fig. 12(a) illustrates a situation in which the grinding depth is much smaller than the SSD1. The maximum grinding temperature is about 250 °C in these grinding parameters. At this temperature, fused silica's ductile machinability is a little improved but not enough to increase the critical depth of brittle–ductile transition significantly. The subsurface damage can be removed partly. However, the cutting force of the grains has exceeded the threshold of crack propagation at the corresponding grinding temperature. Thus material is still removed in an entire brittle mode.

The grinding depth of 3 μm is a little smaller than the subsurface damage depth induced by rough ground in fused silica. Fig. 12(b) illustrates a situation in which the grinding depth is a little smaller than the SSD1. The maximum grinding temperature is 522.5 °C in these grinding parameters. The high grinding temperature can improve shear flow and prevent crack initiation, thus the surface integrity and quality are improved. However, the subsurface damage is not completely removed for the SSD1 is deeper than the grinding depth. The micro cracks which are shallower than the SSD1 are removed while the primary cracks which are deeper than the 1 are left behind and propagate downwards. Therefore, a smaller SSD2 still exists on this condition.

The grinding depth of 5 μm is larger than the subsurface damage depth induced by rough ground in fused silica. Fig. 12(c) illustrates a situation in which the grinding depth is larger than the SSD1. The maximum grinding temperature is 651.1 °C in these grinding parameters. The high grinding temperature improves shear flow and prevent crack initiation and propagation. The subsurface damage is completely removed. A smooth surface without any damage is ground in a superior ductile mode.

Instead of the conventional experience that the brittle–ductile transition occurs with the narrow enough grinding depth, this study concludes a contrary result that lower surface roughness and higher surface integrity is attributed to a large grinding depth. Actually the larger grinding depth corresponding a higher grinding temperature which induces an easier shear flow and prevents cracks initiation and propagation. This result may be related to the more densified molecule structure of fused silica at high temperatures. A high grinding temperature which may improve the fused silica's ductile machinability, and a larger grinding depth than the SSD induced by the previous grinding pass are two prerequisites for dry grinding of fused silica in crack-free ductile mode. However, an exceedingly large grinding depth induces wheel burn, which results in a poor quality and integrity of the ground surface.

4. Conclusion

Fused silica exhibits less densification and more shear flow at high temperature than room temperature. The critical ductile–brittle transition load of fused silica is higher at high temperature than room temperature under the same indentation load. The densified molecules structure at high temperature may lead to the improvement of the fused silica's ductile machinability.

A mathematical model is established to predict the maximum workpiece temperature in contact zone. The maximum workpiece temperature in the grinding zone of different grinding depth was measured precisely by a newly developed infrared radiation (IR) transmission on-line measurement method. The predicted magnitude and variation trend of temperature coincide well with the experiment results.

Because of the increased grinding temperature, lower surface roughness and higher surface integrity are attributed to a large grinding depth in the dry grinding of fused silica; however, an excessive grinding depth results in grinding wheel burn. The ductile grinding depth of fused silica increases from a few submicrometers to 5 μm by the dry grinding process which makes the grinding process more controllable and effective.

A high grinding temperature which improves the fused silica's ductile machinability, and a larger grinding depth than the subsurface damage (SSD) depth induced by the previous grinding pass

are two prerequisites for dry grinding of fused silica in crack-free ductile mode.

Acknowledgments

This study was supported by the National Natural Science Foundation of China (Grant no. 51305237).

References

[1] W. Dai, X. Xiang, Y. Jiang, H.J. Wang, X.B. Li, X.D. Yuan, et al., Surface evolution and laser damage resistance of CO_2, laser irradiated area of fused silica, Opt. Lasers Eng. 49 (2) (2011) 273–280.
[2] C.J. Evans, E. Paul, D. Dornfeld, D.A. Lucca, G. Byrne, M. Tricard, et al., Material removal mechanisms in lapping and polishing, CIRP Ann. – Manuf. Technol. 52 (2) (2003) 611–633.
[3] M. Arif, X. Zhang, M. Rahman, S. Kumar, A predictive model of the critical undeformed chip thickness for ductile–brittle transition in nano-machining of brittle materials, Int. J. Mach. Tools Manuf. 64 (4) (2013) 114–122.
[4] E. Brinksmeier, Y. Mutlugünes, F. Klocke, J.C. Aurich, P. Shore, H. Ohmori, Ultra-precision grinding, CIRP Ann. – Manuf. Technol. 59 (2) (2010) 652–671.
[5] J. Xie, Q. Li, J.X. Sun, Y.H. Li, Study on ductile-mode mirror grinding of sic ceramic freeform surface using an elliptical torus-shaped diamond wheel, J. Mater. Process. Technol. 222 (2015) 422–433.
[6] Q. Zhao, B. Guo, Ultra-precision grinding of optical glasses using mono-layer nickel electroplated coarse-grained diamond wheels. Part 2: investigation of profile and surface grinding, Precis. Eng. 39 (2015) 67–78.
[7] P. Yao, N. Yoshihara, N. Hitomi, J.W. Yan, T. Kuriyagawa, Ductile and brittle mode grinding of fused silica, Key Eng. Mater. 447–448 (2010) 21–25.
[8] Q. Zhao, Y. Liang, D. Stephenson, J. Corbett, Surface and subsurface integrity in diamond grinding of optical glasses on tetraform 'c', Int. J. Mach. Tools Manuf. 47 (14) (2007) 2091–2097.
[9] T.G. Bifano, T.A. Dow, R.O. Scattergood, Ductile-regime grinding: a new technology for machining brittle materials, J. Eng. Ind. 113 (2) (1991) 184–189.
[10] Q. Zhao, L. Zhao, Y. Wang, Q. Meng, High efficient precision conditioning of the electroplated diamond wheel and grinding of fused silica glasses, J. Mech. Eng. 49 (23) (2013) 174–181.
[11] W.K. Neo, A.S. Kumar, M. Rahman, A review on the current research trends in ductile regime machining, Int. J. Adv. Manuf. Technol. 63 (5–8) (2012) 465–480.
[12] M.D. Michel, F.C. Serbena, C.M. Lepienski, Effect of temperature on hardness and indentation cracking of fused silica, J. Non-Cryst. Solids 352 (32–35) (2006) 3550–3555.
[13] M.D. Michel, A. Mikowski, C.M. Lepienski, C.E. Foerster, F.C. Serbena, High temperature microhardness of soda-lime glass, J. Non-Cryst. Solids 348 (22) (2004) 131–138.
[14] K.W. Peter, Densification and flow phenomena of glass in indentation experiments, J. Non-Cryst. Solids 5 (2) (1970) 103–115.
[15] A. Arora, D.B. Marshall, B.R. Lawn, M.V. Swain, Indentation deformation/fracture of normal and anomalous glasses, J. Non-Cryst. Solids 31 (31) (1979) 415–428.
[16] R.F. Cook, G.M. Pharr, Direct observation and analysis of indentation cracking in glasses and ceramics, J. Am. Ceram. Soc. 73 (73) (1990) 787–817.
[17] H.T. Owens, M. Georgiopoulos, M. Belkerdid, Quantitative evaluation of indentation-induced densification in glass, J. Mater. Res. 20 (12) (2005) 3404–3412.
[18] Y. Kato, H. Yamazaki, S. Yoshida, J. Matsuoka, Y. Kato, H. Yamazaki, et al., Effect of densification on crack initiation under vickers indentation test, J. Non-Cryst. Solids 356 (35) (2010) 1768–1773.
[19] C. Hermansen, J. Matsuoka, S. Yoshida, H. Yamazaki, Y. Kato, Y.Z. Yue, Densification and plastic deformation under microindentation in silicate glasses and the relation to hardness and crack resistance, J. Non-Cryst. Solids 364 (1) (2013) 40–43.
[20] P. Sellappan, T. Rouxel, F. Celarie, E. Becker, P. Houizot, R. Conradt, Composition dependence of indentation deformation and indentation cracking in glass, Acta Mater. 61 (16) (2013) 5949–5965.
[21] S. Yoshida, J.C. Sanglebœuf, T. Rouxel, Quantitative evaluation of indentation-induced densification in glass, J. Mater. Res. 20 (12) (2005) 3404–3412.
[22] M.C. Shaw, Principles of Abrasive Processing, Clarendon Press, Oxford University Press, New York, 1996.
[23] R. Brückner, Properties and structure of vitreous silica. i, J. Non-Cryst. Solids 5 (2) (1970) 123–175.
[24] W.C. Oliver, G.M. Pharr, Measurement of hardness and elastic modulus by instrumented indentation: advances in understanding and refinements to methodology, J. Mater. Res. 19 (1) (2004) 3–20.
[25] N. Moharrami, S.J. Bull, A comparison of nanoindentation pile-up in bulk materials and thin films, Thin Solid Films 572 (2014) 189–199.
[26] J.Y. Bei, Analysis and investigation of the grinding temperature, J. Shanghai Jiaotong Univ. 9 (1964) 55–71, in Chinese.
[27] C. Guo, S. Malkin, Analysis of transient temperatures in grinding, J. Eng. Ind. 117 (4) (1995) 571–577.
[28] C. Bus, N. Touwen, P.C. Veenstra, W.V.D. Ach, On the significance of equivalent chip thickness, Ann. CIRP 19 (1971) 121–124.
[29] S. Ramanath, M.C. Shaw, Abrasive grain temperature at the beginning of a cut in fine grinding, J. Eng. Ind. 110 (1) (1988) 15–18.